Computational Condensed Matter 44 (2025) e01108

Contents lists available at ScienceDirect

Computational Condensed Matter

journal homepage: www.elsevier.com/locate/cocom

Full length article

Anharmonic phonon scattering and strain-tunable thermal conductivity in $AlGaAs_2$ DLHC monolayer

Victor José Ramirez Rivera [a], Fredy Mamani Gonzalo [a], José A.S. Laranjeira [b], Nicolas F. Martins [b], Gohnny Acero Laura [c], A.Z. Simoes [c], Julio R. Sambrano [b], Maurício Jeomar Piotrowski [d], Efracio Mamani Flores [a,e,*]

[a] Department of Physics, Jorge Basadre Grohmann National University, Tacna, Peru
[b] Modeling and Molecular Simulation Group, São Paulo State University, Bauru, São Paulo 17033-360, Brazil
[c] School of Engineering and Sciences, São Paulo State University, Guaratinguetá, São Paulo, Brazil
[d] Department of Physics, Federal University of Pelotas, Pelotas, Rio Grande do Sul 96010-900, Brazil
[e] Energy and Materials Research Group (GEM), Jorge Basadre Grohmann National University, Tacna, Peru

ARTICLE INFO

Keywords:
BTT
DLHC
DFT
Monolayer
Phonon transport
Thermoelectric material

ABSTRACT

The emergence of double-layer honeycomb (DLHC) monolayers has broadened the design space of two-dimensional (2D) materials by enabling the stabilization of low-energy configurations of traditional III–V semiconductors. Among them, DLHC-$AlGaAs_2$ has recently attracted attention due to its predicted dynamic and thermodynamic stability, although its physical behavior under strain remains unexplored. In this study, a comprehensive first-principles investigation of the structural, electronic, and phonon transport properties of DLHC-$AlGaAs_2$ under biaxial strain was carried out. The results obtained reveal that strain profoundly influences phonon dynamics: tensile strain increases lattice anharmonicity, reflected in higher Grüneisen parameters and shorter phonon lifetimes, which in turn enhance phonon–phonon scattering. This leads to a notable reduction in lattice thermal conductivity (κ_l) from 3.72 to 3.05 $Wm^{-1}K^{-1}$ as the strain is varied from −2% to +2%. The thermal transport is primarily governed by acoustic phonons, whose group velocities and mean free paths exhibit strong strain dependence. Given its pronounced sensitivity to strain and the resulting tunability of its thermal transport behavior, DLHC-$AlGaAs_2$ emerges as a strong candidate for integration into 2D thermoelectric and nanoscale electronic systems where efficient heat management is essential.

1. Introduction

The increasing global energy demand, along with the detrimental environmental effects of fossil fuels, has accelerated the need for clean, sustainable, and efficient energy conversion technologies [1]. Among the various alternatives, thermoelectric (TE) materials have attracted considerable attention due to their ability to directly convert heat into electrical energy via the Seebeck effect, holding great promise for waste heat harvesting and solid-state cooling technologies [2]. A key challenge in thermoelectric materials development is achieving high conversion efficiency, which is quantified by the dimensionless figure of merit:

$$ZT = \frac{S^2\sigma T}{\kappa}, \tag{1}$$

where S denotes the Seebeck coefficient, σ is the electrical conductivity, T is the absolute temperature, and κ is the total thermal conductivity comprising electronic (κ_e) and lattice (κ_l) contributions. Among these, lowering κ_l without impairing the electronic performance has emerged as a promising strategy to boost ZT [3,4]. To optimize thermoelectric performance, materials should ideally exhibit a large S, σ and low κ_l, which together determine the figure of merit ZT. However, due to intrinsic correlations among these properties, maximizing ZT remains a formidable challenge. For example, materials with wide bandgaps tend to possess higher S values but suffer from reduced carrier mobility and hence lower σ, negatively impacting the power factor. A practical strategy to enhance ZT involves reducing κ_l without degrading electronic transport. This can be achieved through multiple approaches such as enhancing phonon–phonon scattering [5], doping [6,7], incorporating atomic impurities [8], and notably, through mechanical strain engineering. Each of these methods contributes to increased phonon scattering and anharmonicity, thus lowering thermal conductivity and boosting thermoelectric efficiency. Among them, biaxial strain has emerged as a particularly effective route

* Corresponding author at: Department of Physics, Jorge Basadre Grohmann National University, Tacna, Peru.
E-mail address: emamanif@unjbg.edu.pe (E.M. Flores).

https://doi.org/10.1016/j.cocom.2025.e01108
Received 31 May 2025; Received in revised form 4 August 2025; Accepted 5 August 2025
Available online 14 August 2025

for tuning the thermal and electronic behavior of two-dimensional materials [9,10]. It enables precise modulation of the phonon dispersion relations, reduction of phonon group velocities, and shortening of phonon lifetimes, all of which contribute to the suppression of κ_l [11,12]. Simultaneously, strain can also reshape the electronic band structure-modifying the bandgap size and character [13], enhancing carrier effective masses [14,15], or inducing band convergence, thus potentially improving the power factor [16–21]. These dual capabilities make strain engineering a powerful tool for advancing the design of next-generation thermoelectric materials.

Two-dimensional (2D) materials have emerged as leading candidates in thermoelectric applications due to their low thermal conductivity [22,23], high surface-to-volume ratios [24], and quantum confinement effects [25–27]. Since the isolation of graphene in 2004 [28], numerous 2D compounds, including transition metal dichalcogenides (TMDs) [29,30], group III–V semiconductors [31,32], Janus monolayers [33,34] and carbon allotropes [35,36] have been actively studied for applications in electronics [37], optoelectronics [38], catalysis [29], and thermoelectrics [39]. Expanding this landscape, a new class of 2D materials, the double-layer honeycomb (DLHC) structures, introduced by Lucking et al. [40], showing how bulk-like III–V, II–VI, and I–VII semiconductors can stabilize into monolayer configurations with favorable energetics. Several studies have expanded on this concept [41], exploring the DLHC structures of AlP, AlSb, InSb, and CuI, revealing intriguing electronic, piezoelectric, and mechanical properties [42–53]. AlSb, in particular, has been synthesized in its DLHC form [42], further motivating exploration of chemically similar alloys like $AlGaAs_2$, which was recently proposed as a stable DLHC monolayer by Liu et al. [54]. Their study indicates that $AlGaAs_2$ exhibits semiconducting behavior with favorable optoelectronic characteristics. Nonetheless, its vibrational properties and thermal transport characteristics, especially under external strain, remain largely unexplored. Reducing the lattice thermal conductivity κ_l (dominated by phonon transport) without compromising the electronic transport properties is a central strategy in enhancing ZT. This has motivated extensive research into new classes of two-dimensional materials, including not only those exfoliated from bulk layered crystals but also those stabilized in non-traditional ways. For instance, exotic 2D phases such as CuI, which are not stable at room temperature in bulk, have been successfully synthesized through graphene encapsulation techniques, expanding the library of accessible 2D materials [55].

This study presents a comprehensive first-principles analysis of the $AlGaAs_2$ DLHC monolayer, with an emphasis on the modulation of its structural, electronic, and phononic properties under biaxial strain. Mechanical stability was verified through elastic constants, while phonon dispersion relations, group velocities, and phonon lifetimes were systematically analyzed. The lattice thermal conductivity was calculated using the Boltzmann transport formalism. The results obtained indicate that biaxial strain effectively alters phonon transport behavior and significantly suppresses lattice thermal conductivity, positioning $AlGaAs_2$ DLHC monolayer as a promising material for strain-adaptive thermoelectric applications.

2. Computational details

Density functional theory (DFT) was employed for first-principles calculations, using the plane-wave pseudopotential method as implemented in Quantum ESPRESSO [56]. The projector augmented-wave (PAW) method [57] was employed in conjunction with the Perdew–Burke–Ernzerhof (PBE) exchange–correlation functional [58], within the generalized gradient approximation (GGA). To account for long-range dispersion interactions, van der Waals corrections were incorporated using the DFT-D3 method developed by Grimme [59]. In order to address the typical underestimation of bandgaps associated with semi-local functionals, electronic structure refinements were carried out using the hybrid Heyd–Scuseria–Ernzerhof (HSE06) functional [60].

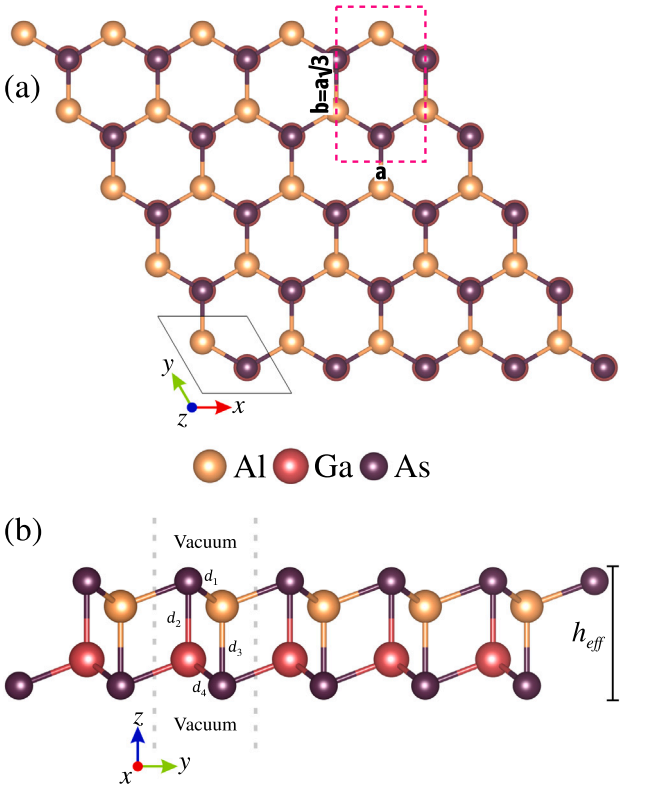

Fig. 1. Top (a) and side (b) perspectives of $AlGaAs_2$ DLHC monolayer are shown. In (a), the unit cell is outlined by the solid black line, while the pink dashed line indicates the orthogonal cell used for the determination of elastic constants. The diagram in (b) depicts the measurements of distances, and heights for the DLHC monolayer. (For interpretation of the references to color in this figure legend, the reader is referred to the web version of this article.)

The Brillouin zone was sampled using a 15 × 15 × 1 Monkhorst–Pack grid, and the plane-wave kinetic energy cutoff was set to 50 Ry. The convergence criterion for total energy during the self-consistent field (SCF) procedure was set to 10^{-12} Ry, and structural relaxations were considered converged when the residual atomic forces were below 10^{-3} Ry/Bohr. Convergence tests related to the energy cutoff and **k**-point density are presented in the Figure S1 in the Supplementary Material (SM). Mechanical properties were assessed via the strain–energy method [61], with full structural optimization performed under each applied strain. The lattice thermal conductivity was evaluated based on both harmonic (second-order) and anharmonic (third-order) interatomic force constants (IFCs). Harmonic IFCs were obtained using the finite displacement approach as implemented in Phonopy [62], employing 8 × 8 × 1 supercells and a 2 × 2 × 1 **k**-point mesh. The Born–Huang symmetry constraints [63] were enforced during the force constant extraction using HiPhive [64]. Anharmonic IFCs were computed with Phono3py [65], using 5 × 5 × 1 supercells and a 2 × 2 × 1 **k**-point grid. Four-phonon scattering was excluded due to its substantially higher computational cost and limited interaction range; thus, only three-phonon processes were considered. Following convergence analysis (Figure S2 in SM), a **Q**-mesh of 85 × 85 × 1 was selected for the solution of the linearized Boltzmann transport equation (LBTE) [66]. A real-space cutoff distance greater than 8.51 Å was used to limit the third-order interaction range. Given the quasi-two-dimensional nature of the system, the out-of-plane lattice thermal conductivity was corrected by applying a normalization factor $L_z = z/h_{\mathrm{eff}}$, where z corresponds to the unit cell length along the z-axis, and h_{eff} is the effective monolayer thickness, estimated by incorporating van der Waals radii of 1.83 Å for arsenic. The in-plane components of the thermal conductivity tensor were used, both x and y directions. To assess thermal stability

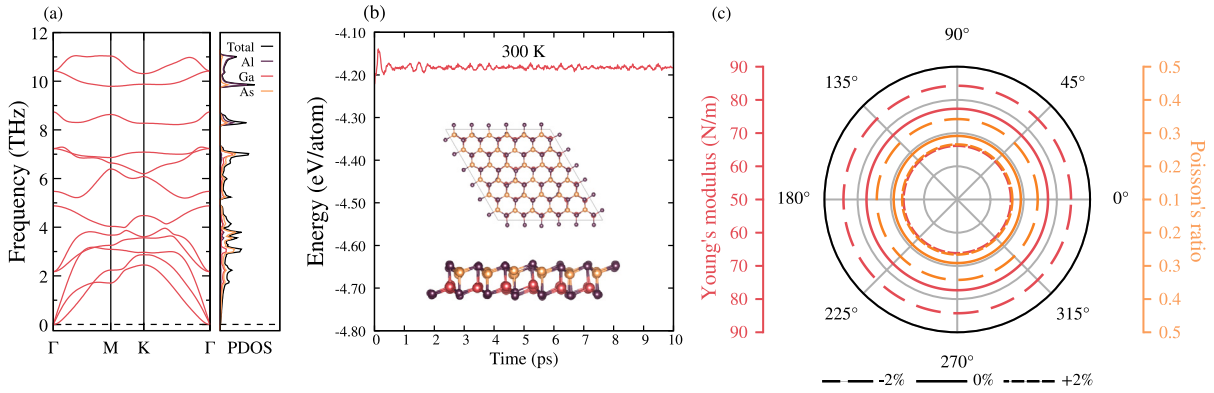

Fig. 2. (a) The calculated phonon dispersions with their respective atomic projected phonon density of states. (b) Ab initio molecular dynamics simulations at 300 K and at 0% of strain. (c) Young's modulus and Poisson's ratio for $AlGaAs_2$ DLHC monolayer under biaxial strain.

Table 1
Calculated lattice constant a (Å), bond lengths d_{1-4} (Å), effective thickness h_{eff} (Å), cohesive energy E_{Coh} (eV/atom), relaxed ion stiffness constants C_{ij}, Young's modulus Y_{2D} (Nm^{-1}) and Poisson's ratio ν for $AlGaAs_2$ DLHC monolayer.

Strain	a	d_1	d_2	d_3	d_4	h_{eff}	E_{Coh}	C_{11}	C_{12}	C_{66}	Y_{2D}	ν
−2%	3.93	2.444	2.696	2.729	2.456	7.30	4.292	95.45	32.67	31.39	84.27	0.342
0%	4.01	2.473	2.685	2.721	2.485	7.25	4.302	84.51	24.63	29.94	77.33	0.291
+2%	4.09	2.505	2.671	2.704	2.516	7.20	4.293	71.21	18.93	26.14	66.18	0.266

and dynamical behavior under finite-temperature conditions, ab initio molecular dynamics (AIMD) simulations were carried out using the Vienna Ab initio Simulation Package (VASP) [67]. Simulations were performed in the canonical (NVT) ensemble on a 6 × 6 × 1 supercell with a Γ-centered **k**-point mesh and an energy cutoff of 400 eV.

3. Results and discussion

3.1. Structural properties

The double-layer honeycomb (DLHC) structure of the $AlGaAs_2$ monolayer crystallizes in the $P\bar{3}m1$ space group (No. 164) and comprises four atomic planes arranged in a puckered bilayer configuration. This geometry aligns with previously reported DLHC structures in other III–V compounds such as AlSb and InAs [42,68]. The structural optimization was carried out at zero strain (0%), and biaxial strains of −2% and +2% were subsequently applied by varying the lattice parameter relative to the relaxed configuration, as depicted in Fig. 1. The top and side views of the relaxed atomic configurations are shown in Fig. 1(a–b), respectively. A rectangular unit cell highlighted by a dashed pink outline was used for obtain mechanical properties. To eliminate spurious interactions between periodic images, a vacuum spacing of 20 Å was included along the out-of-plane (z) direction. At equilibrium (0% strain), the lattice parameter was found to be 4.01 Å, in excellent agreement with the previously reported theoretical value of 4.03 Å by Liu et al. [54], decreasing to 3.93 Å under compressive strain and increasing to 4.09 Å under tensile strain. These changes are accompanied by variations in the bond lengths (d_1–d_4) and the effective monolayer thickness h_{eff}, as summarized in Table 1 and illustrated in Fig. 3(c). Notably, tensile strain slightly reduces h_{eff}, indicating a subtle geometric flattening of the layer.

Biaxial strain significantly modifies the internal bonding environment of the DLHC $AlGaAs_2$ monolayer. As shown in Fig. 1(c), tensile strain induces elongation of bonds d_1 and d_4, while compressing d_2 and d_3. This asymmetric bond response reflects the anisotropic nature of the lattice bonds. The stretching of d_1 and d_4 weakens their corresponding interatomic interactions, reducing the phonon group velocity and enhancing phonon–phonon scattering due to increased anharmonicity. Although the contraction of d_2 and d_3 locally stiffens some modes, it does not offset the overall softening of the lattice. Consequently, the lattice thermal conductivity will decrease with increasing tensile strain.

The thermodynamic stability of $AlGaAs_2$ DLHC monolayer under biaxial strain conditions was assessed by computing the cohesive energy per atom, expressed as:

$$E_{\mathrm{Coh}} = \frac{N_{\mathrm{Al}}E_{\mathrm{Al}} + N_{\mathrm{Ga}}E_{\mathrm{Ga}} + N_{\mathrm{As}}E_{\mathrm{As}} - E_{\mathrm{AlGaAs_2}}}{N_{\mathrm{Al}} + N_{\mathrm{Ga}} + N_{\mathrm{As}}}, \quad (2)$$

where N_i and E_i denote the number and isolated energy of atom species i (Al, Ga, As), respectively, and $E_{\mathrm{AlGaAs_2}}$ is the total energy of the relaxed system. The computed values, listed in Table 1, lie in the narrow range of 4.292–4.302 eV/atom, confirming the energetic stability and strong chemical bonding of the DLHC $AlGaAs_2$ monolayer even under moderate strain.

To assess the dynamical stability of the DLHC $AlGaAs_2$ monolayer, phonon dispersion calculations were performed. As shown in Fig. 2 (a) and Figure S3 in SM, no imaginary frequencies are observed throughout the Brillouin zone, confirming the absence of structural instabilities under the applied biaxial strains. The highest phonon frequencies exhibit a slight variation with strain: 11.46 THz at −2%, 11.04 THz at 0%, and 10.56 THz at +2%. These shifts reflect subtle modifications in the interatomic force constants due to strain-induced structural changes. The vibrational modes can be broadly classified based on atomic mass contributions. Heavier atoms, such as As, tend to dominate the low-frequency acoustic and low-energy optical branches due to their larger inertia. In contrast, the lighter Al atoms predominantly contribute to the high-frequency optical modes. Gallium atoms participate across a broader frequency range, reinforcing the vibrational activity of As atoms in the acoustic region and the lower part of the optical spectrum. Notably, no phonon gap is observed between the acoustic and optical branches, indicating the possibility of significant phonon–phonon scattering processes involving low-frequency modes. This behavior has been previously linked to reduced lattice thermal conductivity in other low-dimensional materials [69–72].

To further verify thermal stability at room temperature, ab initio molecular dynamics (AIMD) simulations were conducted for a 10 ps trajectory, as depicted in Fig. 2(b) and Figure S4 in SM. Throughout the simulation, the system maintains its structural integrity without any observable bond breaking or phase transitions. The total energy fluctuations remain within a stable range, supporting the robustness of the $AlGaAs_2$ monolayer under ambient conditions (see Figure S4 in the Supporting Information for snapshots of the initial and final configurations).

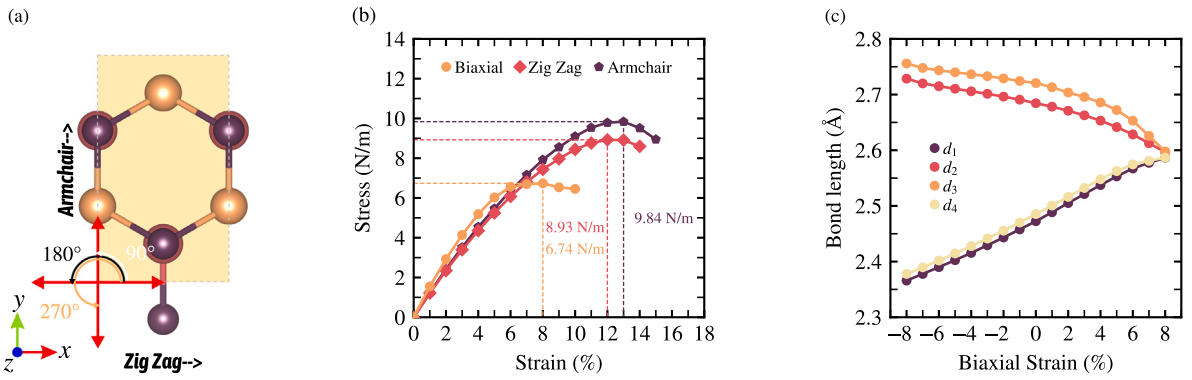

Fig. 3. (a) A diagram showing the top view of $AlGaAs_2$ DLHC monolayer, highlighting the Zigzag and Armchair directions in relation to the rectangular unit cell. (b) Stress under biaxial and uniaxial strain. (c) Bond length d_{1-4} as a function of the biaxial strain.

3.2. Mechanical properties

To evaluate the mechanical characteristics and stability of the DLHC $AlGaAs_2$ monolayer under each strain, the in-plane elastic constants C_{ij} were computed using Voigt notation within a rectangular supercell framework, as depicted in Fig. 1(a). Mechanical deformations were introduced in the form of uniaxial and shear strains, $\varepsilon_{x/y}$ and ε_{xy} respectively, within the range of ±1% at 0.5% intervals. The variation in total energy due to applied strain was used to extract the elastic constants via the strain–energy relation:

$$\frac{\Delta E(S,\varepsilon_i)}{S_0} = \frac{1}{2}\left(C_{11}\varepsilon_{11}^2 + C_{22}\varepsilon_{22}^2 + 2C_{12}\varepsilon_{11}\varepsilon_{22} + 4C_{66}\varepsilon_{12}^2\right), \tag{3}$$

where ΔE denotes the energy difference relative to the equilibrium configuration, S_0 is the relaxed surface area, and ε_{11}, ε_{22}, and ε_{12} represent the normal and shear strain components.

The individual elastic constants were determined by fitting the strain–energy data to the quadratic form, following:

$$C_{11} = \frac{1}{S_0}\frac{\partial^2 U}{\partial \varepsilon_{11}^2}, \quad C_{22} = \frac{1}{S_0}\frac{\partial^2 U}{\partial \varepsilon_{22}^2}, \quad C_{12} = \frac{1}{S_0}\frac{\partial^2 U}{\partial \varepsilon_{11}\partial \varepsilon_{22}}. \tag{4}$$

Given the hexagonal symmetry of the system, the elastic response is isotropic in the plane, meaning $C_{11} = C_{22}$ and $C_{12} = C_{21}$. The shear modulus C_{66} was obtained from the relation $C_{66} = (C_{11} - C_{12})/2$. Accordingly, the stiffness tensor in Voigt notation for such a 2D hexagonal system takes the form:

$$C_{ij} = \begin{pmatrix} C_{11} & C_{12} & 0 \\ C_{12} & C_{11} & 0 \\ 0 & 0 & C_{66} \end{pmatrix}. \tag{5}$$

The mechanical stability of the monolayer was verified using the Born stability criteria for 2D hexagonal lattices [73], which require that $C_{11} > 0$ and $C_{11}^2 > C_{12}^2$. These conditions are met for the structures studied, confirming their mechanical robustness, as reported in Table 1.

Moreover, the computed elastic constants were employed to derive the angular dependence of the in-plane Young's modulus $Y_{2D}(\theta)$ and Poisson's ratio $\nu(\theta)$, which describe the directional stiffness and transverse strain response, respectively:

$$Y_{2D}(\theta) = \frac{C_{11}C_{22} - C_{12}^2}{C_{11}A^4 + C_{22}B^4 - \Lambda A^2 B^2}, \tag{6}$$

$$\nu(\theta) = \frac{C_{11}C_{22} - \Pi A^2 B^2 - C_{12}(A^4 + B^4)}{C_{11}A^4 + C_{22}B^4 + \Pi A^2 B^2}, \tag{7}$$

where θ denotes the direction of measurement with respect to the crystallographic axes, $A = \sin(\theta)$, $B = \cos(\theta)$, and $\Pi = \left[(C_{11}C_{22} - C_{12}^2)/C_{66} - 2C_{12}\right]$. As summarized in Table 1, the $AlGaAs_2$ monolayer displays nearly isotropic mechanical behavior, with minor variations in stiffness under strain. The elastic response of the $AlGaAs_2$ DLHC monolayer under biaxial strain is illustrated in Fig. 3(b–c), where the two-dimensional Young's modulus (Y_{2D}) and Poisson's ratio (ν) are presented as a function of applied strain. At equilibrium (0% strain), the system exhibits a Young's modulus of 77.33 Nm^{-1} and a Poisson's ratio of 0.291. Under compressive (−2%) and tensile (+2%) strain, Y_{2D} increases to 84.27 Nm^{-1} and decreases to 66.18 Nm^{-1}, respectively, while ν shifts slightly to 0.342 and 0.266. These mechanical parameters indicate moderate in-plane stiffness and a relatively low transverse response, suggesting good tolerance to mechanical deformation, and at the same time are close to 74.72 Nm^{-1} obtained by Liu et al. [54] and higher than DLHC-Al_2SbBi monolayer with 48.9 Nm^{-1} [48], however, to further assess the mechanical robustness, the ideal strength and critical strain thresholds were analyzed under stress–strain relation, as shown in Fig. 3(b). The maximum stress under biaxial loading was found to be 6.74 Nm^{-1} at a strain of 8%, indicating good tolerance to uniform expansion. For uniaxial tensile tests, the critical strength reached 8.93 Nm^{-1} at 12% strain along the zigzag direction, and 9.84 Nm^{-1} at 13% along the armchair direction. These results point to a robust mechanical response, particularly under directional strain, and suggest the $AlGaAs_2$ monolayer can endure significant lattice deformation before failure, making it a promising candidate for strain-engineered applications.

3.3. Electronic properties

The electronic structure of the $AlGaAs_2$ DLHC monolayer was initially assessed using the Perdew–Burke–Ernzerhof (PBE) generalized gradient approximation, which offers a qualitative description of the band topology. However, PBE is known to systematically underestimate bandgap values due to inherent self-interaction errors and the absence of a derivative discontinuity. To improve the accuracy of quasiparticle energy predictions, the screened hybrid functional HSE06 was subsequently applied, incorporating a fraction of exact Hartree–Fock exchange and thus providing a more reliable estimate of the electronic bandgap. Fig. 4(a) shows a comparison between the band structures computed using both functionals at equilibrium (0% strain), while Fig. 4(b) presents the orbital-resolved band structure obtained with PBE. According to the HSE06 calculations, the $AlGaAs_2$ monolayer exhibits a direct bandgap of 1.04 eV at the Γ point under equilibrium conditions. This value is consistent with a previous theoretical report by Liu et al. [54], who predicted a gap of 1.05 eV using the same level of theory for the same material. Notably, the PBE functional yields a smaller bandgap of approximately 0.62 eV, highlighting the importance of employing more sophisticated approaches to accurately capture the electronic excitation spectrum.

Table 2
The bandgaps (E_g) calculated using both PBE and HSE06 functionals, along with the vacuum energy (E_{Vac}), the Fermi level (E_F) and the electrostatic potential (Φ) are summarized for $AlGaAs_2$ DLHC monolayer. All values shown are in eV.

Strain	E_g^{PBE}	E_g^{HSE06}	E_{Vac}	E_F	Φ
−2%	0.60	1.43	3.64	−0.79	4.43
0%	0.25	1.04	3.54	−1.38	4.92
+2%	0.00	0.70	3.43	−1.78	5.21

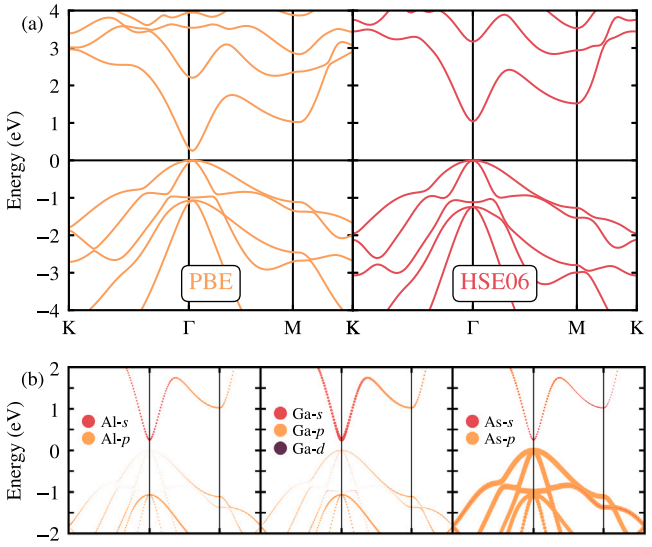

Fig. 4. (a) Electronic band structure of the $AlGaAs_2$ DLHC monolayer at equilibrium, calculated using the PBE and HSE06 functionals. (b) Orbital-projected band structure obtained using the PBE functional.

A detailed orbital-projected analysis reveals that the valence band maximum (VBM) is mainly composed of arsenic p orbitals, particularly the p_z components, reflecting the layered nature of the monolayer and the presence of out-of-plane bonding. Interestingly, the top of the valence band near Γ is not dominated by a single band but rather by the coalescence of two closely spaced bands, which both exhibit strong p-orbital character but differ slightly in their spatial symmetry and elemental contributions. These bands may enable hole mobility anisotropy due to their distinct curvature and effective masses. The conduction band minimum (CBM) is primarily derived from gallium s orbitals, with additional, albeit smaller, contributions from aluminum and arsenic s states, forming a conduction valley that is relatively parabolic and isotropic around the Γ point.

To investigate the influence of mechanical deformation on the electronic structure, biaxial strain was applied in the range of $\epsilon_{xy} = -8\%$ to $+8\%$, and the band structure was recalculated using the HSE06 functional (Fig. 5). The application of compressive strain ($\epsilon_{xy} < 0$) leads to a widening of the bandgap, reaching a maximum value of 1.60 eV at $\epsilon_{xy} = -3\%$. This behavior is associated with an increased interatomic orbital overlap and stronger confinement effects, which push the valence and conduction states further apart. However, beyond this point, a notable change in the band topology occurs: the system undergoes a direct-to-indirect bandgap transition. Although the VBM remains pinned at the Γ point, the CBM migrates away toward the M point in reciprocal space. This shift is due to the differential strain-induced energy level shifts among conduction valleys: while the Γ valley is initially the lowest in energy, it becomes energetically unfavorable under higher compressive stress compared to the emerging local minima near M. Such a transition could significantly affect optical absorption and recombination dynamics, especially in photonic applications.

Conversely, under tensile strain ($\epsilon_{xy} > 0$), the bandgap exhibits a gradual reduction, driven by the elongation of in-plane bond lengths and the associated weakening of orbital hybridization. At $\epsilon_{xy} = +4\%$, the bandgap becomes indirect again, albeit via a different mechanism: the CBM remains at Γ, but the VBM shifts away from Γ toward an intermediate point along the Γ-K direction. This is attributed to the enhanced energy of non-bonding p states that reside between high-symmetry points, favored under tensile conditions. At $\epsilon_{xy} = +8\%$, the separation in momentum space between the VBM and CBM becomes more pronounced, indicating a strong deformation of the electronic landscape and potentially enabling strain-tunable optical transitions.

In addition to the band structure analysis, the electrostatic potential (Φ) was evaluated as a key electronic parameter that quantifies the minimum energy required to extract an electron from the Fermi level to the vacuum level [74]. It is defined as $\Phi = E_{vac} - E_F$, where E_{vac} and E_F denote the vacuum and Fermi energies, respectively (see Fig. 6). For vertically symmetric systems like $AlGaAs_2$, a single vacuum level is sufficient due to structural inversion symmetry. In contrast, systems lacking this symmetry exhibit distinct vacuum levels on opposite surfaces due to intrinsic dipoles and electronegativity gradients. The calculated values of E_{vac}, E_F, and Φ under −2%, 0% and +2% of biaxial strain are summarized in Table 2. At equilibrium, $AlGaAs_2$ presents a work function of 4.92 eV, which increases to 5.21 eV under +2% tensile strain, and decreases to 4.43 eV under −2% compressive strain. These variations are closely related to changes in the surface dipole layer and the redistribution of electron density under deformation. Such tunability of Φ is critical for modulating contact resistance and engineering charge injection barriers in devices like field-effect transistors or Schottky junctions. Moreover, coupling this effect with the strain-driven transition in the bandgap character opens promising avenues for adaptive optoelectronic and straintronic applications.

3.4. Phonon transport properties and lattice thermal conductivity

The evaluation of the lattice contribution to the thermal conductivity of the $AlGaAs_2$ monolayer was conducted through the solution of the linearized Boltzmann transport equation (LBTE), formulated in terms of the Cartesian components $\alpha\beta$ as:

$$\kappa^{\alpha\beta} = \sum_b \frac{1}{k_B T^2 V} \times \left\langle f_0(\omega_{\mathbf{q},b};T)[1+f_0(\omega_{\mathbf{q},b};T)](\hbar\omega_{\mathbf{q},b})^2 v^{\alpha}_{\mathbf{q},b} F^{\beta}_{\mathbf{q},b} \right\rangle_{\mathbf{q}} \quad (8)$$

Here, $\omega_{\mathbf{q},b}$ and $v_{\mathbf{q},b}$ denote the phonon frequency and group velocity, respectively, at wavevector $\mathbf{q}$ for the phonon branch b, while $f_0(\omega_{\mathbf{q},b};T)$ corresponds to the Bose–Einstein distribution at temperature T. The term $F^{\beta}_{\mathbf{q},b}$ encapsulates the components of the nonequilibrium phonon population correction vector, obtained via iterative solution of the LBTE and encoding the phonon scattering processes and relaxation dynamics [75]. The angle brackets $\langle\cdots\rangle_{\mathbf{q}}$ signify an average over the first Brillouin zone.

A crucial quantity derived in this context is the phonon lifetime τ_b, which connects to the scattering rate $\Gamma_b(\omega_b)$ through:

$$v_{\mathbf{q},b} = \frac{\partial\omega_b}{\partial\mathbf{q}} \quad , \quad \tau_b = \frac{1}{2\Gamma_b(\omega_b)} \quad (9)$$

The group velocity is determined from the gradient of the phonon dispersion, and the lifetime τ_b reflects the cumulative impact of phonon–phonon interactions, both harmonic and anharmonic in nature, that contribute to $\Gamma_b(\omega_b)$ similarly to the Fermi golden rule formulation.

Another key metric for assessing anharmonic effects is the Grüneisen parameter $\gamma_b(\mathbf{q})$, which captures the sensitivity of a specific phonon mode to lattice deformation and is given by:

$$\gamma_b(\mathbf{q}) = -\frac{a}{\omega_b}\frac{\partial\omega_b}{\partial a} \quad (10)$$

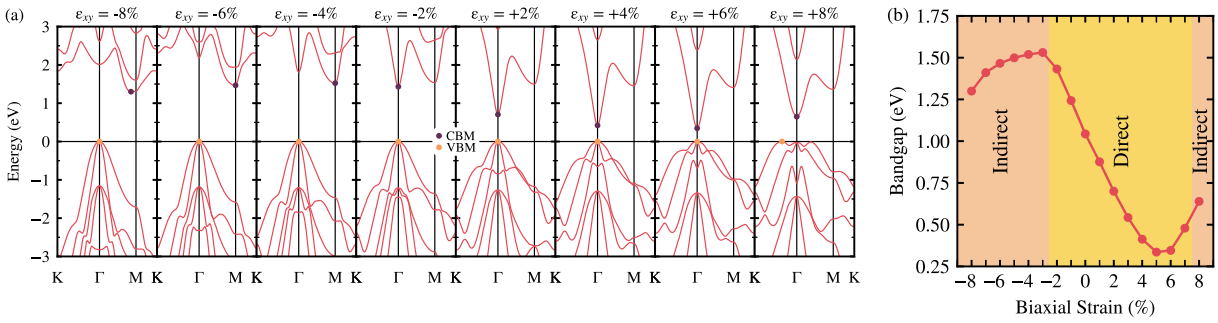

Fig. 5. (a) Evolution of the electronic band structure of the $AlGaAs_2$ monolayer under various biaxial strains using the HSE06 functional. (b) Variation in bandgap value and its direct/indirect character as a function of the applied strain.

Table 3
Average group velocity (km/s), phonon lifetime (ps), Gruneisen parameter and lattice thermal conductivity (Wm^{-1} K^{-1}) for each phonon mode λ for $AlGaAs_2$ DLHC monolayer.

Strain	Group velocity ($\overline{v_\lambda}$)				Phonon lifetime ($\overline{\tau_\lambda}$)				Gruneisen parameter ($\overline{\gamma_\lambda}$)				Lattice thermal conductivity ($\overline{\kappa_\lambda}$)			
	ZA	TA	LA	OPT	ZA	TA	LA	OPT	ZA	TA	LA	OPT	ZA	TA	LA	OPT
−2%	1.58	1.68	1.09	0.72	1.02	2.48	1.70	0.71	1.46	0.47	0.48	0.61	7.16	14.78	10.55	1.03
0%	1.53	1.62	1.16	0.71	1.31	1.80	1.14	0.74	1.02	0.65	0.81	0.66	9.87	11.06	6.87	1.13
+2%	1.48	1.54	1.21	0.70	0.81	0.87	1.26	0.74	1.27	1.18	0.91	1.09	10.64	7.81	7.11	0.95

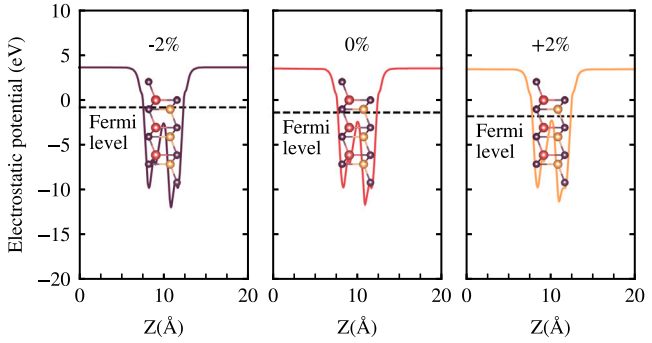

Fig. 6. Work function (Φ) of the $AlGaAs_2$ DLHC monolayer as a function of applied biaxial strain.

Here, a represents the in-plane lattice constant, and a larger averaged magnitude $\overline{|\gamma|}$ typically indicates stronger anharmonic scattering, which impedes phonon transport and reduces lattice thermal conductivity [76].

This framework was applied to the $AlGaAs_2$ monolayer subjected to biaxial strain to quantify how strain-induced phonon softening or hardening, along with modified group velocities and lifetimes, govern the resulting thermal transport behavior. The dependence of these properties on strain is key for tailoring thermal conductivity in 2D semiconductors for thermoelectric or nanoelectronic applications.

Analyzing the group velocity v_g across different biaxial strains in Fig. 7(a), it is evident that acoustic modes consistently contribute more than optical modes, though with strain-dependent variations. For instance, at −2% strain, the average $\overline{v_g}$ values for ZA, TA, LA, and Optical modes are 1.58, 1.68, 1.09, and 0.72 km/s, respectively, with an average across all phonon modes of 0.90 km/s. At 0% strain, these values are slightly altered, with averages of 1.53, 1.62, 1.16, and 0.71 km/s, respectively, resulting in a general $\overline{v_g}$ around 0.89 km/s. Finally, at +2% strain, the velocities for all phonon modes are slightly reduced to 0.88 km/s, while for each phonon mode b are 1.48, 1.54, 1.21, and 0.70 km/s, respectively. The obtained and reported values indicate a moderate increase in the LA mode velocity under tensile biaxial strain, contrasting with the slight reductions observed for the ZA and TA modes. These relatively low average group velocities are conducive to the reduction of the lattice thermal conductivity, κ_l, particularly under tensile strain. For a more comprehensive understanding of the thermal transport behavior, the phonon lifetime τ_b was also analyzed to elucidate the anharmonic effects arising from the absence of a phonon gap between acoustic and optical modes (corresponding values for each phonon mode are provided in Table 3).

Acoustic phonon modes, particularly the TA and LA modes, dominate the phonon lifetimes when compared to the optical modes. Under different biaxial strain conditions, the phonon lifetimes exhibit a clear trend, with acoustic modes generally having longer lifetimes than the optical ones. This behavior further emphasizes the contribution of acoustic modes to the overall phonon dynamics and the observed anharmonicity. The average phonon lifetime $\overline{\tau_b}$ decreases from 0.97 ps at −2% strain to 0.80 ps at +2% strain, suggesting increased anharmonicity with tensile biaxial strain due to enhanced scattering.

Furthermore, the Grüneisen parameter $\overline{|\gamma|}$ observed in Fig. 7(c) is also an indicator of strong anharmonicity, as it is directly related to κ_l in solids. The average values for all phonon modes under −2%, 0%, and +2% strains are 0.65, 0.70, and 1.10, respectively (the corresponding values for each phonon mode can be found in Table 3). These values are in line with materials exhibiting moderate to high anharmonicity, comparable to materials such as BiCuSeO [77] and Bi_2Te_3 [78], which have Grüneisen parameters around ~1.5 and ~1.56, respectively.

As a result of high anharmonicity, a low κ_l is expected. However, before discussing the results obtained for κ_l, it is necessary to implement out-of-plane ZA acoustic mode rotational invariance conditions so that ZA behaves purely quadratically at the Gamma point. This is applied by following the Born–Huang methodology [63] via HiPhive [64], as neglecting such conditions in evaluating κ_l may lead to substantial alterations in lattice thermal conductivity, as seen in Eq. (8), which depends on phonon modes b, and is therefore sensitive to them [79–82]. As shown in Fig. 7(d), at room temperature, κ_l for 0% strain is 3.39 Wm^{-1} K^{-1}, which is notably lower than that of other group III–V monolayer semiconductors, as previously reported in the literature [83, 84]. This trend holds under different biaxial strains, with κ_l values of 3.72, 3.39, and 3.05 Wm^{-1} K^{-1} for −2%, 0%, and +2%, respectively, demonstrating an advantageous balance between thermal conductivity and strain responsiveness, relevant for thermoelectric functionality. Additionally, recent studies have reported similar or even lower values in emerging low-dimensional systems. For instance, La_2GeI_2 exhibits a room-temperature κ_l of 3.22 Wm^{-1} K^{-1}, which can be further reduced to 0.57 Wm^{-1} K^{-1} under external strain [85].

In the DLHC-$AlGaAs_2$ monolayer, phonon mode-resolved analysis reveals that thermal transport is predominantly governed by acoustic phonons, with strain-sensitive contributions. Under compressive strain

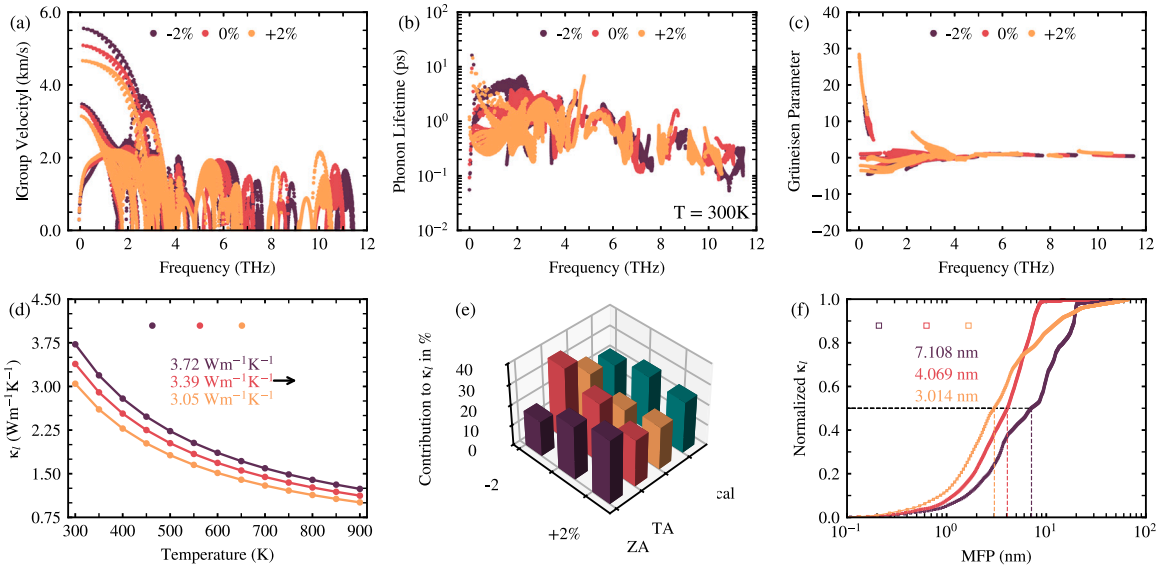

Fig. 7. (a) Group velocity, (b) phonon lifetime, (c) Grüneisen parameter, (d) lattice thermal conductivity as a function of the temperature, (e) contribution of different phonon modes to lattice thermal conductivity and (f) cumulative lattice thermal conductivity versus phonon MFP at 300 K for $AlGaAs_2$ DLHC monolayer under biaxial strain.

(−2%), the transverse acoustic (TA) mode contributes the most to the total lattice thermal conductivity (κ_l), accounting for approximately 35.4%, followed by the longitudinal acoustic (LA, 25.3%) and out-of-plane acoustic (ZA, 17.2%) modes. At equilibrium (0%), the distribution becomes more balanced, with the TA mode still leading (29.2%), but closely followed by optical phonons (26.7%) and ZA modes (26.0%), indicating increased optical mode participation. Under tensile strain (+2%), the ZA mode becomes the dominant contributor (31.2%), while TA and LA contributions drop to 22.9% and 20.8%, respectively. The optical phonon contribution remains relatively stable across strain conditions, ranging between 22% and 27%, indicating a progressive redistribution of heat-carrying phonons from TA/LA modes toward ZA and optical modes under tensile strain. Detailed mode-by-mode contributions are illustrated in Figures S5–S7 in SM.

Moreover, when evaluating and designing nanostructures for thermoelectric applications, it is necessary to know the phonon mean free path (MFP) with respect to cumulative lattice thermal conductivity κ_l^c, which is observed in Fig. 7(f) at 300 K. Here, κ_l^c rises with MFP until it reaches 4.07 nm at 0% strain, signifying the thermodynamic limit, while at compressive (tensile) biaxial strain of −2(+2)% it reaches 7.11 (3.01) nm. It is important to note that a greater contribution of acoustic phonon modes to κ_l leads to a larger MFP, as shown in Fig. 7(e). When the sample size becomes smaller than the phonon mean free path (MFP), the cumulative lattice thermal conductivity κ_l^c experiences a marked reduction. Conversely, as the MFP increases, κ_l^c gradually rises until it approaches the thermodynamic limit. At equilibrium (0% strain), a characteristic MFP of approximately 4.07 nm results in a 50% reduction of κ_l. Under compressive strain (−2%), the characteristic MFP extends to 7.11 nm, while under tensile strain (+2%), it decreases to 3.01 nm. This trend reflects the strong influence of strain on phonon transport, with tensile strain promoting enhanced phonon scattering, suppressing the lattice thermal conductivity, and thereby contributing to improved thermoelectric performance.

4. Conclusions

This study presents a comprehensive theoretical analysis of the biaxial strain effects on the structural, electronic, and phonon transport properties of the $AlGaAs_2$ double-layer honeycomb (DLHC) monolayer, based on first-principles calculations and the linearized Boltzmann transport equation. The results confirm that the material is both dynamically and thermodynamically stable and exhibits a pronounced sensitivity to mechanical deformation. The electronic bandgap can be tuned not only in magnitude but also in nature, transitioning from a direct to an indirect bandgap under moderate compressive or tensile strain, driven by the relative shift of conduction and valence band extrema. Moreover, the work function demonstrates a strain-dependent variation of nearly 0.8 eV, which could be advantageous in interface engineering for electronic devices. In terms of phonon transport, acoustic phonons are found to dominate the heat-carrying mechanisms, with significant contributions from the transverse acoustic (TA) and out-of-plane (ZA) modes. Tensile strain increases phonon–phonon scattering due to enhanced anharmonicity, as indicated by higher Grüneisen parameters and reduced phonon lifetimes. This behavior leads to a clear suppression of the lattice thermal conductivity, with an overall reduction exceeding 18% under +2% strain. Additionally, the phonon mean free paths are shown to be relatively short and further diminish under tensile strain, reinforcing the role of strain as an effective tool to modulate phonon dynamics. These insights position $AlGaAs_2$ DLHC monolayer as a promising platform for strain-engineered phonon transport control in two-dimensional thermoelectric and nanoelectronic applications.

CRediT authorship contribution statement

Victor José Ramirez Rivera: Investigation, Conceptualization. **Fredy Mamani Gonzalo:** Writing – review & editing, Software, Methodology. **José A.S. Laranjeira:** Data curation. **Nicolas F. Martins:** Formal analysis. **Gohnny Acero Laura:** Methodology, Investigation. **A.Z. Simoes:** Investigation. **Julio R. Sambrano:** Investigation. **Maurício Jeomar Piotrowski:** Methodology, Investigation. **Efracio Mamani Flores:** Writing – review & editing, Writing – original draft, Supervision, Project administration, Investigation, Conceptualization.

Funding

This research was made possible by the generous financial support of the Universidad Nacional Jorge Basadre Grohmann, Peru. Funding was provided through the "Fondos del canon, sobrecanon y regalías mineras" program, as approved by Rectoral Resolution N° 11174-2023-UNJBG.

Declaration of competing interest

The authors declare that they have no known competing financial interests or personal relationships that could have appeared to influence the work reported in this paper.

Acknowledgments

We extend our heartfelt gratitude to the Universidad Nacional Jorge Basadre Grohmann for its unwavering support through the projects: "Development of new thermoelectric materials for energy conversion: A theoretical and experimental approach". This project were approved by Rectoral Resolution N° 11174-2023-UNJBG. We would also like to acknowledge the support received from the Rio Grande do Sul Research Foundation (FAPERGS, grant 24/2551-0001551-5), National Council for Scientific and Technological Development (CNPq, grants 307345/2021-1 and 444431/2024-1).

Appendix A. Supplementary data

Supplementary material related to this article can be found online at https://doi.org/10.1016/j.cocom.2025.e01108.

Data availability

No data was used for the research described in the article.

References

[1] D. Gayen, R. Chatterjee, S. Roy, A review on environmental impacts of renewable energy for sustainable development, Int. J. Environ. Sci. Technol. 21 (5) (2024) 5285–5310.
[2] Y. Qin, B. Qin, D. Wang, C. Chang, L.-D. Zhao, Solid-state cooling: thermoelectrics, Energy Environ. Sci. 15 (11) (2022) 4527–4541.
[3] H.A. Eivari, Z. Sohbatzadeh, P. Mele, M. Assadi, Low thermal conductivity: fundamentals and theoretical aspects in thermoelectric applications, Mater. Today Energy 21 (2021) 100744.
[4] C.-D. Zhou, B. Liang, W.-J. Huang, J.-G. Noudem, X.-J. Tan, J. Jiang, Phonon engineering significantly reducing thermal conductivity of thermoelectric materials: a review, Rare Met. 42 (9) (2023) 2825–2839.
[5] L. Yang, Z.-G. Chen, M. Hong, G. Han, J. Zou, Enhanced thermoelectric performance of nanostructured Bi_2Te_3 through significant phonon scattering, ACS Appl. Mater. Interfaces 7 (42) (2015) 23694–23699.
[6] L. Huang, S. Wan, J. Wu, B. Wang, H. Yu, Y. Liu, J. Zhang, Y. Wu, X. Zhang, J. Yan, et al., Triple synergistic modulation via Sn doping in tetrahedrites: Electronic structure, DOS, and scattering engineering for a high thermoelectric performance, ACS Appl. Mater. Interfaces (2025).
[7] B. Kaur, S.A. Khandy, S. Dhiman, M.D. Albaqami, K. Kaur, Thermoelectric properties of Sn_2SSe via band engineering with Ge alloying, Phys. Scr. 99 (9) (2024) 095990.
[8] L. Ramírez-Montes, M.G. Moreno-Armenta, J. Guerrero-Sánchez, R. Ponce-Pérez, R. González-Hernández, W. López-Pérez, Tuning the electronic and thermoelectric properties of selenium monolayers through atomic impurities: A DFT study, Solid State Commun. 371 (2023) 115268.
[9] R. Gupta, S. Kakkar, B. Dongre, J. Carrete, C. Bera, Enhancement in the thermoelectric performance of SnS monolayer by strain engineering, ACS Appl. Energy Mater. 6 (7) (2023) 3944–3952.
[10] Q. Wang, L. Han, L. Wu, T. Zhang, S. Li, P. Lu, Strain effect on thermoelectric performance of InSe monolayer, Nanoscale Res. Lett. 14 (2019) 1–9.
[11] V.J. Ramirez Rivera, F. Mamani Gonzalo, H.E. Nina Mendoza, M. Jeomar Piotrowski, J.A. Chacaltana Garcia, E. Rodrigues Delgado, E. Mamani Flores, Unveiling the impact of biaxial strain on phonon transport in Janus γ-Ge_2SSe monolayer for thermoelectric applications, J. Appl. Phys. 136 (23) (2024).
[12] F.M. Gonzalo, V.J.R. Rivera, M.J. Piotrowski, G.A. Laura, A. Simoes, E.M. Flores, Strain-induced modulation of electronic, optical, and transport properties in PtX_2 (X=S, Se) monolayers, Phys. B 709 (2025) 417191.
[13] H. Liu, Y. Li, R. Chen, Y. Zhao, J. Gao, Strain-tunable electronic anisotropy of the AlSb double-layer honeycomb structure, Phys. Chem. Chem. Phys. 26 (39) (2024) 25664–25669.
[14] J.M.G. Hernandez, J.G. Sanchez, H.N.F. Escamilla, G.H. Cocoletzi, N. Takeuchi, First-principles studies of the strain-induced band-gap tuning in black phosphorene, J. Phys.: Condens. Matter. 33 (17) (2021) 175502.
[15] J.M. Galicia-Hernandez, J. Guerrero-Sanchez, R. Ponce-Perez, H. Fernandez-Escamilla, G.H. Cocoletzi, N. Takeuchi, Self-energy corrected band-gap tuning induced by strain in the hexagonal boron phosphide monolayer, Comput. Mater. Sci. 203 (2022) 111144.
[16] F.M. Gonzalo, V.J.R. Rivera, J.R. Sambrano, M.J. Piotrowski, E.M. Flores, Strain-tunable electronic, optical and thermoelectric properties of two-dimensional Janus SbXI (X=S, Se, Te) monolayers: A first-principles study, Results Phys. 74 (2025) 108288.
[17] W. Ibarra-Hernández, A. Garcia-Castro, A. Bautista-Hernández, M. Salazar-Villanueva, A. Cantarero, A.H. Romero, Modification of electronic and thermoelectric properties of InSe/GaSe superlattices by strain engineering, Phys. Rev. Mater. 6 (2) (2022) 025403.
[18] S. Bai, S. Tang, M. Wu, D. Luo, J. Zhang, D. Wan, S. Yang, Unravelling the thermoelectric properties and suppression of bipolar effect under strain engineering for the asymmetric Janus SnSSe and PbSSe monolayers, Appl. Surf. Sci. 599 (2022) 153962.
[19] J. Ma, F. Meng, J. He, Y. Jia, W. Li, Strain-induced ultrahigh electron mobility and thermoelectric figure of merit in monolayer α-Te, ACS Appl. Mater. Interfaces 12 (39) (2020) 43901–43910.
[20] E.M. Flores, V.J.R. Rivera, E.J.S. Sacari, J.R. Sambrano, M.L. Moreira, M.J. Piotrowski, Biaxial strain effects on electronic, transport, and thermoelectric properties of SnX_2 (X=Se, Te) and Janus SnSeTe 1T-monolayers, Mater. Today Commun. 39 (2024) 108830.
[21] R.R. Banik, S. Ghosh, J. Chowdhury, Strain induced modulations in the thermoelectric properties of 2D SiH and GeH monolayers: insights from first-principle calculations, J. Phys.: Condens. Matter. 36 (25) (2024) 255706.
[22] J. Wu, Y. Chen, J. Wu, K. Hippalgaonkar, Perspectives on thermoelectricity in layered and 2D materials, Adv. Electron. Mater. 4 (12) (2018) 1800248.
[23] D. Li, Y. Gong, Y. Chen, J. Lin, Q. Khan, Y. Zhang, Y. Li, H. Zhang, H. Xie, Recent progress of two-dimensional thermoelectric materials, Nano-Micro Lett. 12 (2020) 1–40.
[24] F.K. Perkins, A.L. Friedman, E. Cobas, P. Campbell, G. Jernigan, B.T. Jonker, Chemical vapor sensing with monolayer MoS_2, Nano Lett. 13 (2) (2013) 668–673.
[25] Z. Gan, L. Liu, H. Wu, Y. Hao, Y. Shan, X. Wu, P.K. Chu, Quantum confinement effects across two-dimensional planes in MoS_2 quantum dots, Appl. Phys. Lett. 106 (23) (2015).
[26] G.Y. Jia, Y. Liu, J.Y. Gong, D.Y. Lei, D.L. Wang, Z.X. Huang, Excitonic quantum confinement modified optical conductivity of monolayer and few-layered MoS_2, J. Mater. Chem. C 4 (37) (2016) 8822–8828.
[27] J.G. Roch, N. Leisgang, G. Froehlicher, P. Makk, K. Watanabe, T. Taniguchi, C. Schonenberger, R.J. Warburton, Quantum-confined stark effect in a MoS_2 monolayer van der Waals heterostructure, Nano Lett. 18 (2) (2018) 1070–1074.
[28] K.S. Novoselov, A.K. Geim, S.V. Morozov, D.-e. Jiang, Y. Zhang, S.V. Dubonos, I.V. Grigorieva, A.A. Firsov, Electric field effect in atomically thin carbon films, Science 306 (5696) (2004) 666–669.
[29] M. Chhowalla, H.S. Shin, G. Eda, L.-J. Li, K.P. Loh, H. Zhang, The chemistry of two-dimensional layered transition metal dichalcogenide nanosheets, Nat. Chem. 5 (4) (2013) 263–275.
[30] A. Ayari, E. Cobas, O. Ogundadegbe, M.S. Fuhrer, Realization and electrical characterization of ultrathin crystals of layered transition-metal dichalcogenides, J. Appl. Phys. 101 (1) (2007).
[31] H. Şahin, S. Cahangirov, M. Topsakal, E. Bekaroglu, E. Akturk, R.T. Senger, S. Ciraci, Monolayer honeycomb structures of group-IV elements and III-V binary compounds: First-principles calculations, Phys. Rev. B—Condens. Matter Mater. Phys. 80 (15) (2009) 155453.
[32] T. Suzuki, Theoretical discovery of stable structures of group III-V monolayers: The materials for semiconductor devices, Appl. Phys. Lett. 107 (21) (2015).
[33] J. Zhang, S. Jia, I. Kholmanov, L. Dong, D. Er, W. Chen, H. Guo, Z. Jin, V.B. Shenoy, L. Shi, et al., Janus monolayer transition-metal dichalcogenides, ACS Nano 11 (8) (2017) 8192–8198.
[34] A.-Y. Lu, H. Zhu, J. Xiao, C.-P. Chuu, Y. Han, M.-H. Chiu, C.-C. Cheng, C.-W. Yang, K.-H. Wei, Y. Yang, et al., Janus monolayers of transition metal dichalcogenides, Nature Nanotechnology 12 (8) (2017) 744–749.
[35] J.A. Laranjeira, N. Martins, P.A. Denis, J. Sambrano, Unveiling a new 2D semiconductor: Biphenylene-based InN, ACS Omega 9 (26) (2024) 28879–28887.
[36] N.F. Martins, A.S. Maia, J.A. Laranjeira, G.S. Fabris, A.R. Albuquerque, J.R. Sambrano, Hydrogen storage on the lithium and sodium-decorated inorganic graphenylene, Int. J. Hydrog. Energy 51 (2024) 98–107.
[37] G. Fiori, F. Bonaccorso, G. Iannaccone, T. Palacios, D. Neumaier, A. Seabaugh, S.K. Banerjee, L. Colombo, Electronics based on two-dimensional materials, Nature Nanotechnology 9 (10) (2014) 768–779.
[38] D. Jariwala, V.K. Sangwan, L.J. Lauhon, T.J. Marks, M.C. Hersam, Emerging device applications for semiconducting two-dimensional transition metal dichalcogenides, ACS Nano 8 (2) (2014) 1102–1120.
[39] M. Fronzi, P. Mele, A.V. Ellis, C. Stampfl, Advances in van der Waals thermoelectric materials: Prospects and challenges, RSC Appl. Interfaces (2025).
[40] M.C. Lucking, W. Xie, D.-H. Choe, D. West, T.-M. Lu, S. Zhang, Traditional semiconductors in the two-dimensional limit, Phys. Rev. Lett. 120 (8) (2018) 086101.

[41] M.-Y. Ma, D. Han, N.-K. Chen, D. Wang, X.-B. Li, Recent progress in double-layer honeycomb structure: A new type of two-dimensional material, Materials 15 (21) (2022) 7715.

[42] L. Qin, Z.-H. Zhang, Z. Jiang, K. Fan, W.-H. Zhang, Q.-Y. Tang, H.-N. Xia, F. Meng, Q. Zhang, L. Gu, et al., Realization of AlSb in the double-layer honeycomb structure: a robust class of two-dimensional material, ACS Nano 15 (5) (2021) 8184–8191.

[43] A. Bafekry, M. Faraji, M. Fadlallah, H. Jappor, S. Karbasizadeh, M. Ghergherehchi, I.A. Sarsari, A.A. Ziabari, Novel two-dimensional AlSb and InSb monolayers with a double-layer honeycomb structure: a first-principles study, Phys. Chem. Chem. Phys. 23 (34) (2021) 18752–18759.

[44] A. Bafekry, M. Faraji, S. Karbasizadeh, H. Jappor, I.A. Sarsari, M. Ghergherehchi, D. Gogova, Investigation of vacancy defects and substitutional doping in AlSb monolayer with double layer honeycomb structure: a first-principles calculation, J. Phys.: Condens. Matter. 34 (6) (2021) 065701.

[45] A. Bafekry, M. Faraji, S. Fazeli, S. H. Khan, M. Fadlallah, C. Stampfl, M. Ghergherehchi, G. Chang, B. Shokri, Controlling the electro-optical properties of an AlSb monolayer with a DLHC structure through phosphorus alloying: a DFT study, J. Phys. Chem. C 128 (19) (2024) 8016–8024.

[46] M.A. Mohebpour, M.B. Tagani, First-principles study on the electronic and optical properties of AlSb monolayer, Sci. Rep. 13 (1) (2023) 9925.

[47] S. Dong, Y. Li, Excitonic instability and electronic properties of AlSb in the two-dimensional limit, Phys. Rev. B 104 (8) (2021) 085133.

[48] D. Fang, H. Zhang, D. Wang, Two-dimensional topological insulator Al_2SbBi with a double-layer honeycomb structure with large spin splitting and piezoelectricity for spintronic devices, ACS Appl. Nano Mater. 6 (18) (2023) 16595–16603.

[49] A. Demirok, H. Sahin, M. Yagmurcukardes, Ultra-thin double-layered hexagonal CuI: strain tunable properties and robust semiconducting behavior, J. Phys.: Condens. Matter. 36 (21) (2024) 215401.

[50] H.-J. Wang, J.-T. Yang, C.-J. Xu, H.-M. Huang, Q. Min, Y.-C. Xiong, S.-J. Luo, Investigations on structural, electronic and optical properties of ZnO in two-dimensional configurations by first-principles calculations, J. Phys.: Condens. Matter. 35 (1) (2022) 014002.

[51] H. Wang, F. Xu, S. Dai, S. Xiao, Z. Yu, Z. Tian, Electronic, optical and photocatalytic water splitting properties of two-dimensional monolayers of Janus Cd_2XY (X=S, Se; Y=Se, Te; X≠Y): a first-principles study, Phys. Scr. 100 (3) (2025) 035921.

[52] S. Yi, G. Liu, Z. Liu, W. Hu, H. Deng, Double-layer honeycomb AlP: a promising anode material for Li-, Na-, and K-ion batteries, J. Phys. Chem. C 124 (5) (2020) 2978–2986.

[53] M.-Y. Ma, N.-K. Chen, D. Wang, D. Han, H.-B. Sun, S. Zhang, X.-B. Li, Defect physics in 2D monolayer I-VII semiconductor AgI, Mater. Today Nano 22 (2023) 100304.

[54] Y. Liu, T. Gao, G. Qian, X. Tan, S. Dai, Y. Gao, L. Li, Q. Xie, Q. Chen, J. Wang, Structural, electronic, and photocatalytic water splitting in two-dimensional monolayer MNXY (M/N=Al, Ga, X/Y=N, P, As) semiconductors: A first-principles perspective, Phys. Rev. B 108 (24) (2023) 245424.

[55] K. Mustonen, C. Hofer, P. Kotrusz, A. Markevich, M. Hulman, C. Mangler, T. Susi, T.J. Pennycook, K. Hricovini, C. Richter, J.C. Meyer, J. Kotakoski, V. Skákalová, Toward exotic layered materials: 2D cuprous iodide, Adv. Mater. 34 (9) (2022) 2106922.

[56] P. Giannozzi, S. Baroni, N. Bonini, M. Calandra, R. Car, C. Cavazzoni, D. Ceresoli, G.L. Chiarotti, M. Cococcioni, I. Dabo, et al., QUANTUM ESPRESSO: a modular and open-source software project for quantum simulations of materials, J. Phys.: Condens. Matter. 21 (39) (2009) 395502.

[57] P.E. Blöchl, Projector augmented-wave method, Phys. Rev. B 50 (24) (1994) 17953.

[58] M. Ernzerhof, G.E. Scuseria, Assessment of the Perdew–Burke–Ernzerhof exchange-correlation functional, J. Chem. Phys. 110 (11) (1999) 5029–5036.

[59] J. Moellmann, S. Grimme, DFT-D3 study of some molecular crystals, J. Phys. Chem. C 118 (14) (2014) 7615–7621.

[60] J. Heyd, G.E. Scuseria, M. Ernzerhof, Hybrid functionals based on a screened Coulomb potential, J. Chem. Phys. 118 (18) (2003) 8207–8215.

[61] S. Thomas, K. Ajith, M. Valsakumar, Directional anisotropy, finite size effect and elastic properties of hexagonal boron nitride, J. Phys.: Condens. Matter. 28 (29) (2016) 295302.

[62] A. Togo, I. Tanaka, First principles phonon calculations in materials science, Scr. Mater. 108 (2015) 1–5.

[63] M. Born, K. Huang, Dynamical Theory of Crystal Lattices, Oxford University Press, 1996.

[64] F. Eriksson, E. Fransson, P. Erhart, The Hiphive Package for the extraction of high-order force constants by machine learning, Adv. Theory Simul. 2 (5) (2019) 1800184.

[65] A. Togo, L. Chaput, T. Tadano, I. Tanaka, Implementation strategies in Phonopy and Phono3py, J. Phys.: Condens. Matter. (2023).

[66] L. Chaput, Direct solution to the linearized phonon Boltzmann equation, Phys. Rev. Lett. 110 (26) (2013) 265506.

[67] J. Hafner, Ab-initio simulations of materials using VASP: Density-functional theory and beyond, J. Comput. Chem. 29 (13) (2008) 2044–2078.

[68] S. Ahmed, A. Jalil, S.Z. Ilyas, H. Mufti, S. Agathopoulos, The first-principles prediction of two-dimensional indium-arsenide bilayers, Mater. Sci. Semicond. Process. 134 (2021) 106041.

[69] C. Hu, L. Zhou, X. Hu, B. Lv, Z. Gao, Mechanism of the low thermal conductivity in novel two-dimensional NaCuSe, Appl. Surf. Sci. 613 (2023) 156064.

[70] M.K. Jana, K. Pal, A. Warankar, P. Mandal, U.V. Waghmare, K. Biswas, Intrinsic rattler-induced low thermal conductivity in Zintl Type $TlInTe_2$, J. Am. Chem. Soc. 139 (12) (2017) 4350–4353.

[71] P.-Z. Jia, Z.-X. Xie, Y.-X. Deng, Y. Zhang, L.-M. Tang, W.-X. Zhou, K.-Q. Chen, High thermoelectric performance induced by strong anharmonic effects in monolayer $(PbX)_2$ (X=S, Se, Te), Appl. Phys. Lett. 121 (4) (2022) 043901.

[72] Q. Xia, Z. Xu, L. Hu, Y. Liu, G. Gao, Ultralow lattice thermal conductivity in bulk and monolayer TlCuSe: a comparative study from first-principles, J. Phys. D: Appl. Phys. 56 (47) (2023) 475304.

[73] M. Maździarz, Comment on 'The computational 2D materials database: high-throughput modeling and discovery of atomically thin crystals', 2D Mater. 6 (4) (2019) 048001.

[74] P.C. Rusu, G. Brocks, Work functions of self-assembled monolayers on metal surfaces by first-principles calculations, Phys. Rev. B—Condens. Matter Mater. Phys. 74 (7) (2006) 073414.

[75] L. Chaput, A. Togo, I. Tanaka, G. Hug, Phonon-phonon interactions in transition metals, Phys. Rev. B 84 (9) (2011) 094302.

[76] C.H. Lee, C.K. Gan, Anharmonic interatomic force constants and thermal conductivity from Grüneisen parameters: An application to graphene, Phys. Rev. B 96 (3) (2017) 035105.

[77] Y.-L. Pei, J. He, J.-F. Li, F. Li, Q. Liu, W. Pan, C. Barreteau, D. Berardan, N. Dragoe, L.-D. Zhao, High thermoelectric performance of oxyselenides: intrinsically low thermal conductivity of Ca-doped BiCuSeO, NPG Asia Mater. 5 (5) (2013) e47–e47.

[78] A.F. Zurhelle, V.L. Deringer, R.P. Stoffel, R. Dronskowski, Ab initio lattice dynamics and thermochemistry of layered bismuth telluride (Bi_2Te_3), J. Phys.: Condens. Matter. 28 (11) (2016) 115401.

[79] J. Carrete, W. Li, L. Lindsay, D.A. Broido, L.J. Gallego, N. Mingo, Physically founded phonon dispersions of few-layer materials and the case of borophene, Mater. Res. Lett. 4 (4) (2016) 204–211.

[80] A. Taheri, S. Pisana, C.V. Singh, Importance of quadratic dispersion in acoustic flexural phonons for thermal transport of two-dimensional materials, Phys. Rev. B 103 (23) (2021) 235426.

[81] C. Lin, S. Poncé, N. Marzari, General invariance and equilibrium conditions for lattice dynamics in 1D, 2D, and 3D materials, Npj Comput. Mater. 8 (1) (2022) 236.

[82] A. Croy, Bending rigidities and universality of flexural modes in 2D crystals, J. Phys.: Mater. 3 (2) (2020) 02LT03.

[83] M. Kourra, K. Sadki, L. Drissi, M. Bousmina, Mechanical response, thermal conductivity and phononic properties of group III-V 2D hexagonal compounds, Mater. Chem. Phys. 267 (2021) 124685.

[84] Y. Hu, D. Li, Y. Yin, S. Li, H. Zhou, G. Zhang, High thermal conductivity driven by the unusual phonon relaxation time platform in 2D monolayer boron arsenide, RSC Adv. 10 (42) (2020) 25305–25310.

[85] S.A. Khandy, K. Kaur, S. Marutheeswaran, I. Islam, Understanding the ultralow thermal conductivity and strong anharmonicity of a lanthanum-based germanium halide monolayer for possible thermoelectric applications, ACS Appl. Energy Mater. 7 (20) (2024) 9279–9288.